Understanding the mechanisms of amorphous creep through molecular simulation

Penghui Cao[a], Michael P. Short[a], and Sidney Yip[a,b,1]

[a]Department of Nuclear Science and Engineering, Massachusetts Institute of Technology, Cambridge, MA 02139; and [b]Department of Materials Science and Engineering, Massachusetts Institute of Technology, Cambridge, MA 02139

Edited by Sharon C. Glotzer, University of Michigan, Ann Arbor, MI, and approved October 27, 2017 (received for review May 24, 2017)

Molecular processes of creep in metallic glass thin films are simulated at experimental timescales using a metadynamics-based atomistic method. Space–time evolutions of the atomic strains and nonaffine atom displacements are analyzed to reveal details of the atomic-level deformation and flow processes of amorphous creep in response to stress and thermal activations. From the simulation results, resolved spatially on the nanoscale and temporally over time increments of fractions of a second, we derive a mechanistic explanation of the well-known variation of creep rate with stress. We also construct a deformation map delineating the predominant regimes of diffusional creep at low stress and high temperature and deformational creep at high stress. Our findings validate the relevance of two original models of the mechanisms of amorphous plasticity: one focusing on atomic diffusion via free volume and the other focusing on stress-induced shear deformation. These processes are found to be nonlinearly coupled through dynamically heterogeneous fluctuations that characterize the slow dynamics of systems out of equilibrium.

creep | molecular simulation | deformation mechanism | atomistic modeling | metallic glass

Deformation and flow are fundamental in the rheological behavior of many materials (1–4). For the molecular understanding of plastic response under stress (creep), a standing challenge is to know the details by which the constituent atoms rearrange themselves individually and collectively in a local environment of stress and temperature. Creep experiments have been extensively reported on amorphous materials, including metallic glasses and colloidal systems (5–9). Yet, the relationship between stress and temperature effects on creep and the underlying microscopic processes remains an open question. Theoretical models have been proposed to describe the mechanisms of molecular deformation and flow responsible for amorphous plasticity. Spaepen (10) considered the distinction between homogeneous and inhomogeneous flows in metallic glasses and introduced the concept of the local free volume as an order parameter. In this view, local strain production and dissipation are assumed to be associated with individual atomic jumps. Argon (11) proposed a plastic deformation model of metallic glasses based on the notion of local shear transformations driven by stress and in the presence of thermal fluctuations. The atoms participating in such processes essentially undergo an inelastic shear deformation. Falk and Langer (12) later introduced the term shear transformation zone (STZ) in interpreting simulation results of viscoplastic deformation of amorphous solids. The STZ theory was further extended to be capable of describing temperature- and rate-dependent amorphous plasticity (13, 14). The term STZ has become widely adopted in studies of amorphous materials. (4, 8, 15–20).

We seek to identify the elementary processes of deformation and flow in amorphous creep through atomistic simulation. A bottleneck well-known in the literature is that the temporal scales relevant to creep are beyond the reach of traditional molecular dynamics (MD). To compensate for its inherently microscopic timescales, MD simulations of creep had to resort to extreme conditions of stress, temperature, and strain rate (21, 22). Here, we implement a metadynamics formulation that allows transition-state trajectories to be generated on appreciably longer timescales on the order of fractions of seconds. By analyzing the distributions of atomic strain and nonaffine particle displacement, we observe the effects of stress and temperature on the evolution of activated states at the microscale. We find that the processes of single-particle diffusion and of shear deformation of small clusters of particles are both active in steady-state creep; in particular, their interplay gives rise to a characteristic upturn behavior of stress effects on creep rate. The simulation results also support a mechanism map showing a regime of low stress and high temperature where diffusional creep dominates and a high-stress regime governed by shear deformation creep. Our findings suggest that, while the two original models of amorphous plasticity (10, 11) are complementary in their individual focus, their combined effects need to be analyzed using more fundamental theories capable of treating the effects of nonlinear feedback.

Simulation Methods and Model

We consider a model $Cu_{50}Zr_{50}$ metallic glass system in two dimensions. The atoms interact through a Lennard–Jones potential (23, 24), which has been used to study plastic deformation (25) and thermally activated flows in metallic glass (26). Two amorphous structures with different sizes, 39.5 × 19.7 nm (containing 10,000 atoms) and 62.5 × 31.2 nm (25,000 atoms), are prepared by quenching from a high-temperature liquid state (*Materials and Methods* has additional details). We apply uniaxial tensile stress to the system and follow the procedure described in *Materials and Methods* to simulate the time evolution of creep.

Significance

The individual and collective molecular displacements in an amorphous solid undergoing plastic deformation are simulated by an atomistic method that allows incremental motions to be observed over a time window of fractions of seconds. Because the timescale matches well with the conditions of experimental measurements, simulation details provide dynamical evidence for the fundamental mechanisms of amorphous creep. In particular, knowledge of the interplay between diffusion (flow) and mechanical deformation processes enables us to explain the stress and temperature behavior of the experimental data as well as the validity of model descriptions of molecular mechanisms in terms of spatially and temporally heterogeneous fluctuations.

Author contributions: P.C. and S.Y. designed research; P.C. performed research; P.C., M.P.S., and S.Y. analyzed data; and P.C., M.P.S., and S.Y. wrote the paper.

The authors declare no conflict of interest.

This article is a PNAS Direct Submission.

[1]To whom correspondence should be addressed. Email: syip@mit.edu.

This article contains supporting information online at www.pnas.org/lookup/suppl/doi:10.1073/pnas.1708618114/-/DCSupplemental.

The algorithms allow us to investigate creep strain evolution and the corresponding molecular mechanisms at various stresses and temperatures, in particular at low stress and slow creep rate. To quantify the atomic-level plastic deformations in creep, we compute two local strains: deviatoric strain D^2_{min} and von Mises strain η_{Mises}. In addition, we compute nonaffine displacement as a measure of single-particle dynamics. Detailed descriptions of atomic strains and displacement are discussed in *Materials and Methods*. We find negligible system size effects on the results; therefore, our discussions will refer to the larger system unless explicitly stated otherwise.

Creep Curves

Fig. 1 shows the time development of the system strain determined by metadynamics simulation. The creep curve shows the classical behavior of three stages of strain evolution. The initial period of strain nucleation and distribution, consisting of a steep increase followed by a gradual approach to saturation, is known as primary or transient creep. The secondary stage of steady-state creep is a period of linear strain increase in time. The extent of this stage depends on the combination of applied stress and system temperature. For relatively low stresses, the secondary stage may have a considerable extent before the onset of tertiary creep, where the strain rate increases without apparent limit (Fig. 2). In the case of Fig. 1, the onset of structural instability at a strain level of $\sim$2.5% is readily observed. Notice that the relevant timescale of creep is of the order of fractions of seconds, comparable with those of laboratory measurements and beyond the capabilities of traditional MD.

Fig. 2 shows a series of creep curves spanning the stress range from 42 to 258 MPa simulated at a temperature of $0.68\,T_g$. At low stresses, one sees only the primary and secondary stages of creep during the simulation. For these cases, the creep rate given by the slope in the secondary stage is sufficiently small that the system remains in steady-state creep throughout the simulation. In contrast, for the two highest stresses, one sees the onset of tertiary creep. While our interest is in the mechanisms sustaining steady-state creep, nevertheless, it is pertinent to note that tertiary creep will be triggered by the appearance and persistent growth of a localized region of high strain, leading to structural instability (failure) of the system (a discussion of atomic strains evolution in creep is in *Supporting Information*) (8, 27).

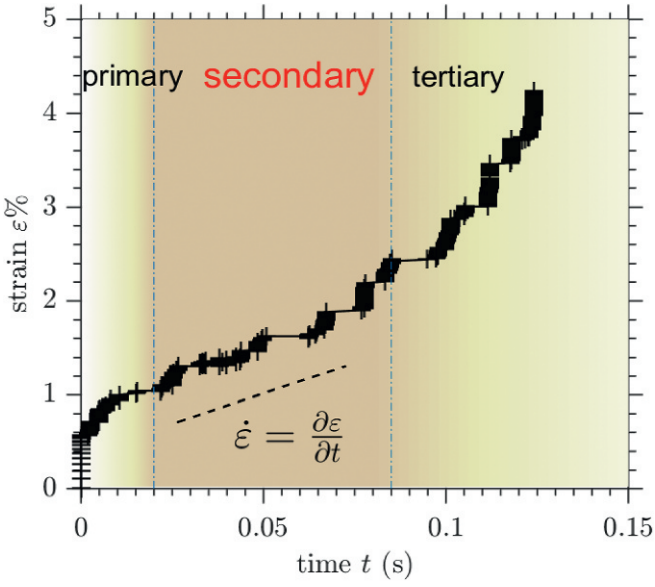

Fig. 1. Simulated creep curve: time evolution of system strain ε at stress 198 MPa and temperature $0.68T_g$. The creep rate $\dot{\varepsilon}$ of the secondary stage is essentially constant and at a minimum. The background colors are drawn schematically to denote the creep rate.

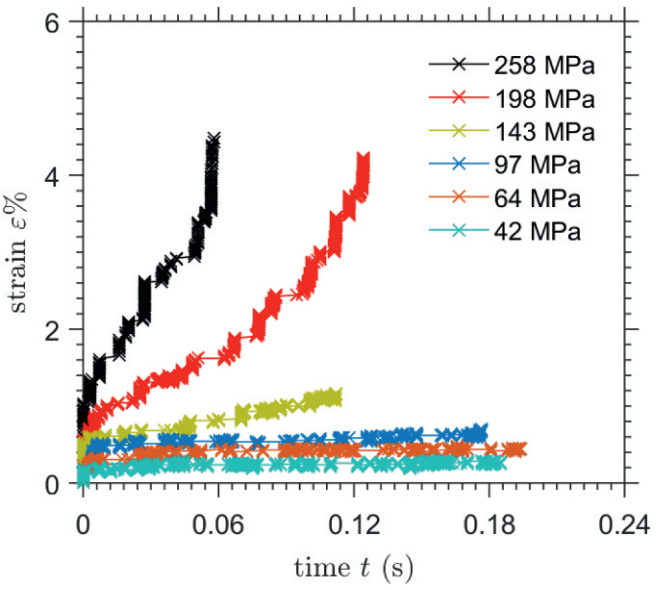

Fig. 2. Simulated creep curves at indicated stress levels at a temperature of $0.68T_g$.

Nonaffine Displacement and Deviatoric Strain Distributions (Dynamical Heterogeneities)

Fig. 2 indicates that the applied stress has a significant effect on the time evolution of the creep (system-level) strain. One can ask for the atomic rearrangements and displacements associated with the observed deformation. In Fig. 3, we show how the probability distributions of nonaffine particle displacement δx in the tensile direction vary with stress. Each distribution is seen to be composed of a Gaussian core and exponentially varying wings. This behavior has been observed previously both in simulations (22, 28) and in experiments (29) of glassy materials close to jamming and glass transitions. They have been interpreted as local fluctuations known as dynamical heterogeneities. Here, as stress increases, we observe that the exponential wings become broader and that a significantly larger fraction of atoms undergoes large displacement. The increasingly more pronounced non-Gaussian behavior can be interpreted as stress-reinforced dynamical heterogeneities. The coexistence of atoms moving appreciably faster or slower than the average is regarded as a characteristic attribute of space–time fluctuations in driven systems. From inspection of Fig. 3, one can also see a change in the overall shape of the probability distributions starting from 143 MPa.

The nonaffine displacement δx plays the role of a dynamical order parameter for single-particle diffusion. Similarly, the atomic strains, η_{Mises} and D^2_{min}, could be associated with local collective deformation. We will focus on D^2_{min} as a more discriminating indicator for local plastic rearrangement (a discussion of D^2_{min} and η_{Mises} is in *Supporting Information*). Fig. 4 shows the variation with stress of the distributions of D^2_{min}. The distributions of small D^2_{min} follow a power law decay with different exponents, and at large D^2_{min}, the distributions show a fall off that is decidedly slower for larger stress, implying more numerous activations of high-strain sites. Fig. 4, *Inset* shows that the number of atoms participating in large strain deformation indeed increases sharply with increasing stress. Corresponding to the stress regime separation noted in Fig. 3, an appreciable increase in the number

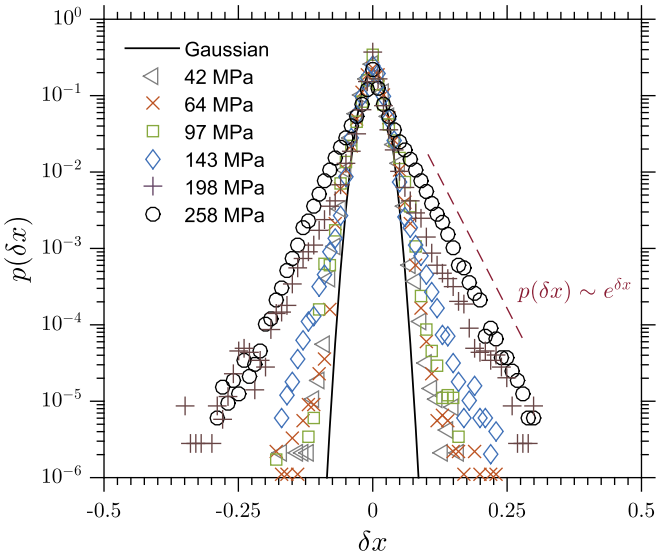

Fig. 3. Statistical distributions of nonaffine particle displacement $p(\delta x)$ at $0.68T_g$ and the various stresses indicated. The solid line represents the fitted Gaussian function, whereas the dashed line is exponential function used to guide the eye. The displacements δx are measured with a time interval of $\delta t = 0.01$ s.

of atoms involved in shear transformations is seen starting at a stress of 143 MPa. This suggests that stress plays a fundamental role in the physical manifestation of deformation and flow behavior in driven systems.

To see what molecular mechanisms could be associated with Figs. 3 and 4, we show in Fig. 5 the local space–time distributions. The spatial maps are resolved at the nanoscale and temporally measured over a time interval of 0.01 s. Maps of nonaffine displacements δx are shown in Fig. 5 *A* and *B*. Correspondingly, maps of D^2_{min} (local deformation) are seen in Fig. 5 *C* and *D*. Fig. 5 *A* and *C* refers to low (64 MPa) stress, and Fig. 5 *B* and *D* for high (258 MPa) stress.

In Fig. 5*A*, the features of the nonaffine displacement map can be essentially attributed to thermally activated atomic diffusion, as initially proposed by Spaepen (10). It could serve as the baseline for measuring responses through single-particle displacements at higher stress. Fig. 5*B* indicates that the displacement magnitude of the sites of high mobility is about a factor of three larger than the displacements at low stress. Moreover, we see the presence of bidirectional flow (red–blue interface in Fig. 5*B*), as several such active zones appear along the 45° direction. When looking at Fig. 5*D*, these activated events appear as local strain bursts, a striking effect of stress-induced deformation. We regard this to be a specific simulation result, obtained at a physically meaningful timescale, that illustrates the synergistic effects of stress activation.

In Fig. 5*C*, we see little or no local shear deformation activity, which suggests that thermally diffusional rearrangements at the temperature of the simulation produce relatively small local plastic strain. These weak events seem quite random in space and do not align in any particular direction. We conclude that, at low stress, creep proceeds mostly by single-particle diffusion rather than cooperative atom deformation. However, at high stress, Fig. 5 *B* and *D* implies that diffusive and deformation processes are both activated and coupled through heterogeneous stress fields in the driven system.

We apply the above findings to predict the variation of creep rate with tensile stress, a behavior of fundamental interest in the mechanics and physics of creep (30, 31). At very low stress, we expect the effects of thermal activation to dominate, which should lead to a mild increase of creep rate with stress. As stress increases, both flow and deformation mechanisms contribute smoothly until the stress exceeds a threshold, at which point thermal and stress activations accelerate. The significant increase in shear transformation deformation events, shown in Fig. 4, *Inset* and the gap noted in Figs. 3 and 4, are hallmarks of a threshold (cross-over) behavior that is widely observed in experiments (Fig. 6*B*). We consider this stress threshold to reveal a regime of nonlinear response, which has not been previously interpreted at the molecular level.

Creep Rate Upturn

The simulated creep curves allow us to determine a steady-state creep rate at each stress. Plotting the results in Fig. 6*A*, we see a bimodal behavior in the monotonic variation of creep rate $\dot{\varepsilon}$ with stress σ, a behavior visible in both the large and small systems. At low stress, $\dot{\varepsilon}$ is characterized by a creep rate slope of $n \sim 1.5$, where n is known as the stress exponent. At high stress, n increases to ~5. Notice that the stress value for the change in index n coincides with the stress gap mentioned in the discussions of Figs. 3 and 4. The transition in creep rate behavior is well-known in experiments on different materials (32–34). It is generally understood to signify thermal activation processes at low stress, changing over to stress activation for reasons that have not yet been resolved particularly regarding the roles of atomic diffusion and shear deformation.

To compare our results with experiments, the simulation data are shown again in Fig. 6*B* along with two sets of measurements (9, 33). Reduced stress σ/σ_0 and strain rate $\dot{\varepsilon}/\dot{\varepsilon}_0$ are plotted, where σ_0 and $\dot{\varepsilon}_0$ are threshold values for creep rate upturn. The upturn in creep rate indicated by the simulation data matches well with the experiments. Our discussions concerning Figs. 3–5 lead us to interpret the creep rate behavior as evidence of the nonlinear response involving the coupling of the atomic diffusion and shear transformation deformation.

Creep Mechanism Map

The creep simulations that we have conducted cover three temperatures, 0.57, 0.68, and $0.91T_g$, and stress values ranging

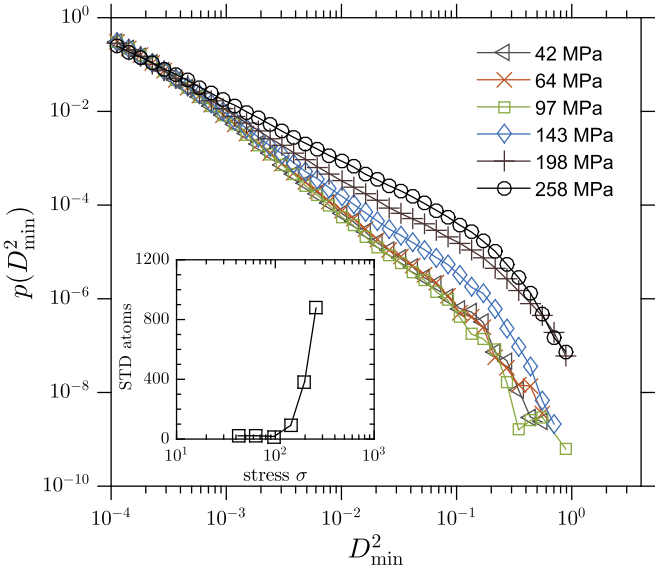

Fig. 4. Statistical distributions of deviatoric strain $p(D^2_{min})$ at a temperature of $0.68T_g$ and the various stresses indicated. The strains are calculated with the time interval $\delta t = 0.01$ s. *Inset* shows variation of the number of shear transformation deformation (STD) atoms with strain that is larger than 0.05.

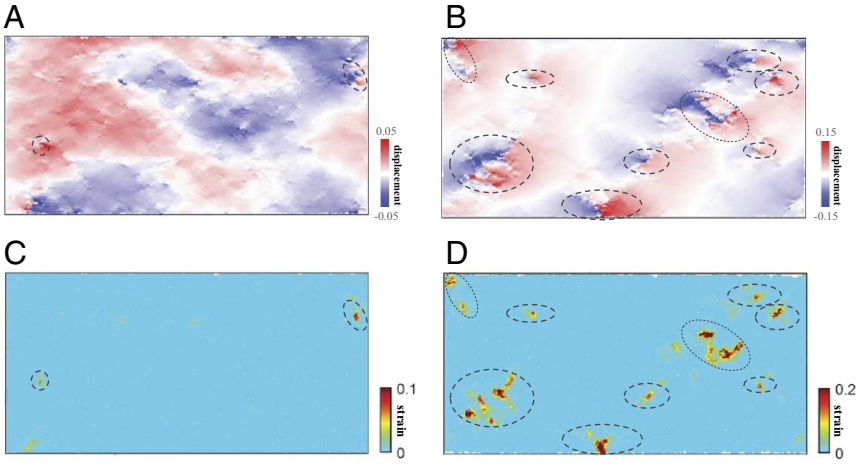

Fig. 5. Spatial distributions of nonaffine displacement (*A* and *B*) and of deviatoric strain (*C* and *D*). All measures are time incremental taken over a time interval of 0.01 s. Atoms are colored according to the magnitude of their displacements or strains. At each level, *A* and *C* denote low stress (64 MPa), and *B* and *D* denote high stress (258 MPa).

from 15 to 290 MPa. At each temperature, a stress-dependent creep rate (the rate for steady-state creep) curve was obtained, from which the stress exponent n was determined. The stress–temperature values of our simulations are plotted in Fig. 7 using squares and circles to denote whether the corresponding value of n is ~ 1 or > 5, respectively. Fig. 7 is effectively a creep mechanism map for our model metallic glass. It delineates the stress–temperature regimes, where single-particle diffusion and shear transformation deformation are the limiting behaviors.

Looking at the simulation data across the temperature range, one can visualize a mechanism boundary separating the map into two domains, where either diffusion or shear deformation predominates. To motivate such a boundary, we recall well-known empirical expressions based on transition-state theory for the limiting behavior of strain rate in amorphous systems. At low stress, the creep rate $\dot{\varepsilon}$ is written in the form (10)

$$\dot{\varepsilon} = \gamma_0 \cdot \exp(-\frac{Q_d}{kT})\frac{V_d}{kT}\sigma, \qquad [1]$$

where Q_d and V_d are the activation energy and activation volume for diffusion, respectively. This is derived based on the free volume diffusion model. At high stress, a more appropriate form is (8, 11)

$$\dot{\varepsilon} = \gamma_0 \cdot \exp\left(-\frac{Q_{st} - \sigma V_{st}}{kT}\right), \qquad [2]$$

where the subscript st denotes shear transformation. This is compatible with the shear transformation deformation model. Setting Eq. **1** equal to Eq. **2** and treating these activation parameters numerically, we find the locus of (σ, T) values for the mechanism boundary to be essentially a straight line: $\sigma(T) = a + bT$ (*Supporting Information* has details). The red dashed curve in Fig. 7 is drawn having this functional form and adjusted to separate the groups of squares and circles. Thus, the simulation data are able to accommodate a boundary that would have the two limiting behaviors described by Eqs. **1** and **2**.

For experimental validation, we show in Fig. 7 mechanical deformation measurements on a five-component metallic glass (9). Except for an overall shift, the experimental and simulation results both display the same predominant domains of diffusional and deformational creep. One can offer only qualitative reasons why a comparison between this simulation and experiment should be considered meaningful. For example, differences between the simulation system and the experimental samples can be quite significant. These could arise from their respective preparations, such as cooling rate and casting defects and surface polish imperfections. Another factor is that an idealized 2D binary mixture model is being compared with measurements on a 3D five-component material. Although a 2D model could be capable of capturing aspects of thermally activated diffusion and stress-induced shear transformation processes, one could argue that the system dimensionality could affect activation energy

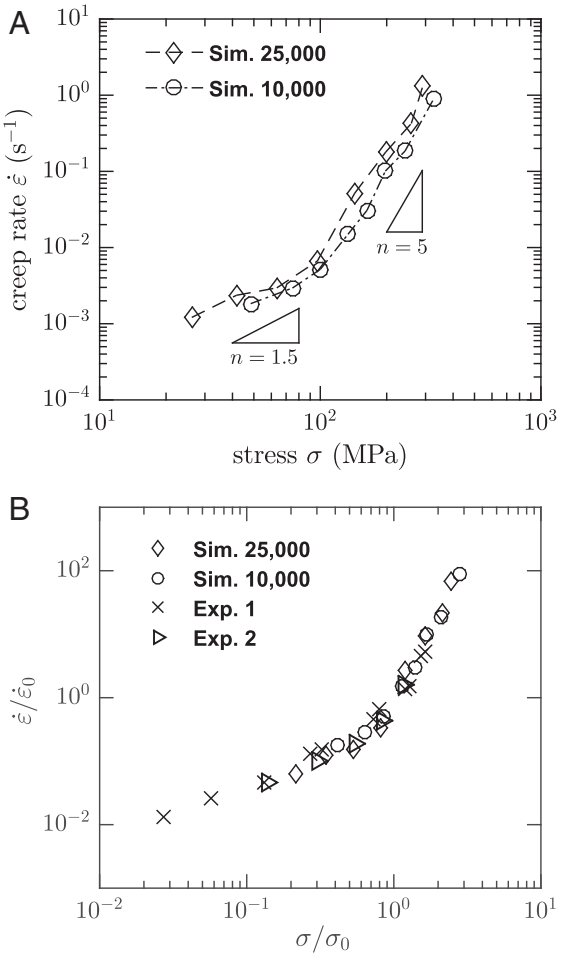

Fig. 6. (*A*) Stress dependence of creep rate from simulations with two different system sizes of 25,000 and 10,000 atoms. (*B*) Stress variation of creep rate. The two sets of experimental data 1 (crosses) and 2 (triangles) are adapted from refs. 9 and 33, respectively; σ_0 and $\dot{\varepsilon}_0$ are threshold values in the creep rate–stress curve.

barriers of elementary processes, which in turn, could influence the creep rate. In addition, the cooling rate in sample preparation will affect the underlying potential energy landscape, and therefore the creep rate response. Indeed, we have performed additional simulations at a cooling rate three orders of magnitude higher and found the mechanism boundary to shift downward in a manner that brings experiments and simulations in Fig. 7 closer together (a discussion of cooling rate is in *Supporting Information*). Other than sample preparation, the shift of the mechanism boundary also may be rationalized by noting that different spatial correlation lengths are involved in single-particle jumps vs. collective distortions of particle clusters, the former being more short-ranged and therefore less cooling-rate sensitive than the latter (35).

Discussion

In this work, we relate the simulation results to the mechanisms proposed by Spaepen (10) and by Argon (11), because each provides a clear-cut physical description for identifying the molecular processes governing creep under varying stress and temperature conditions. An appropriate next step would be to connect the simulation results to theoretical analysis, such as the STZ concept of plastic deformation in amorphous materials. The term STZ, initially conceived to describe a transient flow defect, has evolved as a statistical thermodynamics-based theoretical description of system-level response in a thermal and stress environment. The original theory (12) has been reformulated (14), reviewed (36), and updated (37). At the this time, STZ seems to play two different roles: a mechanism combining the ideas of Spaepen (10) and Argon (8, 11, 38) or a theoretical framework for interpreting experiments or simulations (39, 40).

In discussing Fig. 6, we have regarded the creep rate upturn as signifying the synergistic actions involving single-particle diffusion and shear-induced deformation. One can imagine quantifying this interpretation by using STZ theory to explicitly calculate the creep rate response to stress. Recently, Langer (37) has reported a study of a similar problem, in which the density of STZs and an effective thermodynamic temperature were introduced as dynamical variables in a set of coupled equations of motion with a stress-dependent deformation rate.

We believe that the increase of the stress exponent from approximately two to five delineates a regime of nonlinear response in the rheological behavior of amorphous materials, a consequence of the nonlinear coupling between atomic diffusion and shear-induced deformation. More generally, it indicates an interplay between thermal and stress-activated processes, involving loading effects, thermal noise, and stress-induced fluctuations (41).

In summary, we present findings to quantify the molecular mechanisms of steady-state creep in a model metallic glass. At low stress and high temperature, the dominant mechanism is observed to be thermally activated particle flow, while at high stress, the mechanism is a more complex process of stress-induced enhanced local shear deformation and atomic diffusion. Taking these processes together leads to an interpretation of the experimentally observed stress and temperature behavior of amorphous creep as well as a unifying picture of single-particle diffusion and collective atom rearrangements. This perspective motivates revisiting the existing notion of dynamical heterogeneities (42–44) and a variant of self-organization in slowly driven threshold systems (45) in the spirit of assessing various theoretical frameworks, such as the STZ theory (37), expanded mode-coupling formalism (46), mean field approaches with weakening mechanism (47), and time-dependent transition theory modeling (48).

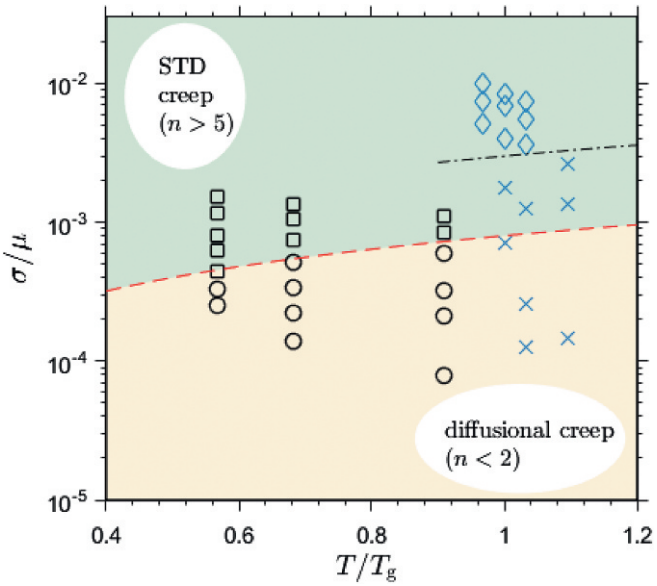

Fig. 7. Creep mechanism map showing normalized stress–temperature regions of dominance; μ represents the elastic modulus of materials. Simulation data are denoted as circles ($n < 2$) and squares ($n > 5$). The boundary separating the predominant shear transformation deformation (STD) mechanism from atomic diffusion mechanism regions is indicated by the red dashed curve. Also shown are experimental data (9) with diamonds ($n > 5$) and crosses ($n \sim 1$).

Materials and Methods

Model Metallic Glass. To prepare the metallic glass thin film configuration for atomistic simulations, we quench from a high-temperature, well-equilibrated liquid state at 0.14 K/ps at zero pressure using MD with periodic boundary conditions in all directions. We observe an inflection point in the volume–temperature curve at 440 K, which is regarded as the glass transition temperature T_g (*Supporting Information*). To model a uniaxial stress experiment, two free surfaces in the *y*-direction are created by removing periodic boundary conditions, so that the stress is free in that direction. We perform another 400-ps MD simulation to relax the system to zero average stress. The mechanical properties of the thin film, such as elastic modulus and yield strength, are then characterized (*Supporting Information*).

Metadynamics Simulation of Creep. To simulate creep using a metadynamics algorithm, we apply a prescribed uniaxial tensile stress to the system and execute the following steps.

i) Perform energy minimization on the relaxed system to bring it to the nearest local energy minimum.
ii) Apply the autonomous basin climbing (ABC) algorithm (49, 50) to obtain the transition-state pathway and determine the neighboring local energy minimum state.
iii) Compare the internal stress of the new state with the prescribed tensile stress. If the two stresses deviate by more than 1%, perform step *iv*; otherwise, go back to step *ii*.
iv) Perform cell relaxation in the presence of the external stress. The atoms are rescaled to new positions whenever the size of simulation cell is changed, and the final configuration converges to a new local minimum.

The output of ABC is a set of transition-state pathway trajectories, each being an ordered sequence of energy minima and saddle points. The system evolution is then determined by examining the newly sampled configurations of the local energy minima. The activation time of each evolution step is estimated through transition-state theory, $\Delta t_i = [\nu_0 \exp(-\frac{\Delta E_i}{k_B T})]^{-1}$, with the attempt frequency ν_0 typically taken to be 10^{12} s^{-1}. ΔE_i is the energy barrier of activation path *i*. ΔE_i could be overestimated by ABC, and therefore, we use the nudged elastic band method (51) to refine the barrier connecting the two neighboring energy minima. The metadynamics simulation is terminated when either tertiary failure occurs or 15,000 activation pathways have been explored.

Atomic-Level Strain and Nonaffine Displacement. We consider two atomic-level strains, the deviatoric strain D^2_{min} and the local von Mises strain η_{Mises},

as measures of local plastic deformation (12, 52). Imagine that a region surrounding an atom undergoes a strain deformation during a time interval δt. The deviatoric strain is defined as

$$D^2_{min}(\delta t) = \sum_{i=1}^{n} [\mathbf{X}_i(t+\delta t) - \mathbf{X}_0(t+\delta t) - \mathbf{J} \times (\mathbf{X}_i(t) - \mathbf{X}_0(t))]^2, \quad [3]$$

where $\mathbf{X}(t)$ is the reference configuration at time t, $\mathbf{X}(t+\delta t)$ is the current configuration at time $t+\delta t$, and the index i runs over all atoms within the interaction cutoff relative to the reference position of atom zero. $\mathbf{J}$ is the affine deformation tensor that transforms a nearest neighbor separation, $\mathbf{X}_i(t) - \mathbf{X}_0(t)$, to what would be expected under an affine deformation. The deformation tensor $\mathbf{J}$ is determined by minimizing D^2_{min}, with the minimum value being the atomic-level deviatoric strain. For each $\mathbf{J}$, a Green strain tensor $\boldsymbol{\eta}$ can be written as $\boldsymbol{\eta} = 1/2(\mathbf{J} \bullet \mathbf{J}^T - \mathbf{I})$. The local atomic strain invariant η_{Mises} in two dimensions is computed by

$$\eta_{Mises} = \sqrt{\eta^2_{xy} + \frac{\eta^2_{xx} + \eta^2_{yy} - \eta^2_{xx}\eta^2_{yy}}{3}}. \quad [4]$$

Note that η_{Mises} is directly derived from $\mathbf{J}$, while D^2_{min} is a measure of the deviation from deformation tensor $\mathbf{J}$. The atomic strains η_{Mises} and D^2_{min} are computed by considering all of the n neighboring atoms. Both can serve as an indicator for cooperative local rearrangement.

The nonaffine displacement is useful for tracking single-atom dynamics. For a time interval (t, $t+\delta t$), it is defined as

$$\delta u_\alpha(t, t+\delta t) = X_\alpha(t+\delta t) - F_{\alpha\beta}X_\beta(t), \quad [5]$$

where the Greek indices α and β indicate the Cartesian components and the deformation gradient F is related to the system-level creep strain $\varepsilon_{\alpha\beta}$ by $F_{\alpha\beta} = 1 + [\varepsilon_{\alpha\beta}(t+\delta t) - \varepsilon_{\alpha\beta}(t)] = 1 + \Delta\varepsilon_{\alpha\beta}(t, t+\delta t)$. In the simulation, the nonaffine displacement in the tensile direction δx is calculated for characterization of single-atom dynamics.

ACKNOWLEDGMENTS. We thank A. S. Argon, J. S. Langer, and K. Kamrin for discussions, and the Massachusetts Institute of Technology (MIT) Nuclear Science and Engineering Department for computational resources. P.C. was supported by US Department of Energy (DOE) Grant DE-NE0008450. M.P.S. was supported by National Science Foundation CAREER Grant DMR-1654548. S.Y. was supported by DOE-Basic Energy Sciences Grant DE-SC0002633 and the Kuwait-MIT Center Signature Project. S.Y. is a founding member of the MIT Concrete Sustainability Hub.

1. Mason T, Bibette J, Weitz D (1996) Yielding and flow of monodisperse emulsions. *J Colloid Interface Sci* 179:439–448.
2. Johnson WL, Lu J, Demetriou MD (2002) Deformation and flow in bulk metallic glasses and deeply undercooled glass forming liquids-a self consistent dynamic free volume model. *Intermetallics* 10:1039–1046.
3. Debregeas G, Tabuteau H, Di Meglio JM (2001) Deformation and flow of a two-dimensional foam under continuous shear. *Phys Rev Lett* 87:178305.
4. Schall P, Weitz DA, Spaepen F (2007) Structural rearrangements that govern flow in colloidal glasses. *Science* 318:1895–1899.
5. Krisponeit JO, et al. (2014) Crossover from random three-dimensional avalanches to correlated nano shear bands in metallic glasses. *Nat Commun* 5:3616.
6. Huang Y, Shen J, Chiu Y, Chen J, Sun J (2009) Indentation creep of an Fe-based bulk metallic glass. *Intermetallics* 17:190–194.
7. Siebenbürger M, Ballauff M, Voigtmann T (2012) Creep in colloidal glasses. *Phys Rev Lett* 108:255701.
8. Schuh CA, Hufnagel TC, Ramamurty U (2007) Mechanical behavior of amorphous alloys. *Acta Mater* 55:4067–4109.
9. Lu J, Ravichandran G, Johnson WL (2003) Deformation behavior of the Zr 41.2 Ti 13.8 Cu 12.5 Ni 10 Be 22.5 bulk metallic glass over a wide range of strain-rates and temperatures. *Acta Mater* 51:3429–3443.
10. Spaepen F (1977) A microscopic mechanism for steady state inhomogeneous flow in metallic glasses. *Acta Metall* 25:407–415.
11. Argon AS (1979) Plastic deformation in metallic glasses. *Acta Metall* 27:47–58.
12. Falk ML, Langer JS (1998) Dynamics of viscoplastic deformation in amorphous solids. *Phys Rev E* 57:7192–7205.
13. Falk M, Langer J, Pechenik L (2004) Thermal effects in the shear-transformation-zone theory of amorphous plasticity: Comparisons to metallic glass data. *Phys Rev E* 70:011507.
14. Bouchbinder E, Langer J (2009) Nonequilibrium thermodynamics of driven amorphous materials.II. Effective-temperature theory. *Phys Rev E* 80:031132.
15. Mayr S (2006) Activation energy of shear transformation zones: A key for understanding rheology of glasses and liquids. *Phys Rev Lett* 97:195501.
16. Tanguy A, Leonforte F, Barrat JL (2006) Plastic response of a 2D Lennard-Jones amorphous solid: Detailed analysis of the local rearrangements at very slow strain rate. *Eur Phys J E* 20:355–364.
17. Pan D, Inoue A, Sakurai T, Chen M (2008) Experimental characterization of shear transformation zones for plastic flow of bulk metallic glasses. *Proc Natl Acad Sci USA* 105:14769–14772.
18. Cao P, Park HS, Lin X (2013) Strain-rate and temperature-driven transition in the shear transformation zone for two-dimensional amorphous solids. *Phys Rev E* 88:042404.
19. Greer A, Cheng Y, Ma E (2013) Shear bands in metallic glasses. *Mater Sci Eng R Rep* 74:71–132.
20. Cao P, Lin X, Park HS (2014) Surface shear-transformation zones in amorphous solids. *Phys Rev E* 90:012311.
21. Yamakov V, Wolf D, Phillpot SR, Mukherjee AK, Gleiter H (2002) Dislocation processes in the deformation of nanocrystalline aluminium by molecular-dynamics simulation. *Nat Mater* 1:45–49.
22. Sentjabrskaja T, et al. (2015) Creep and flow of glasses: Strain response linked to the spatial distribution of dynamical heterogeneities. *Sci Rep* 5:11884.
23. Kobayashi S, Maeda K, Takeuchi S (1980) Computer simulation of deformation of amorphous Cu57Zr43. *Acta Metall* 28:1641–1652.
24. Deng D, Argon A, Yip S (1989) A molecular dynamics model of melting and glass transition in an idealized two-dimensional material I. *Philos Trans R Math Phys Eng Sci* 329:549–573.
25. Schuh CA, Lund AC (2003) Atomistic basis for the plastic yield criterion of metallic glass. *Nat Mater* 2:449–452.
26. Rodney D, Schuh C (2009) Distribution of thermally activated plastic events in a flowing glass. *Phys Rev Lett* 102:235503.
27. Cao A, Cheng Y, Ma E (2009) Structural processes that initiate shear localization in metallic glass. *Acta Mater* 57:5146–5155.
28. Chaudhuri P, Berthier L, Kob W (2007) Universal nature of particle displacements close to glass and jamming transitions. *Phys Rev Lett* 99:060604.
29. Weeks ER, Crocker JC, Levitt AC, Schofield A, Weitz DA (2000) Three-dimensional direct imaging of structural relaxation near the colloidal glass transition. *Science* 287:627–631.
30. Cottrell AH (1953) *Dislocations and Plastic Flow in Crystals* (Clarendon, Oxford).
31. Nabarro FRN, De Villiers F (1995) *Physics of Creep and Creep-Resistant Alloys* (CRC, Boca Raton, FL).
32. Boyle JT, Spence J (2013) *Stress Analysis for Creep* (Elsevier, Amsterdam).
33. Nieh T, Wadsworth J (2006) Homogeneous deformation of bulk metallic glasses. *Scr Mater* 54:387–392.
34. Klueh R (2005) Elevated temperature ferritic and martensitic steels and their application to future nuclear reactors. *Int Mater Rev* 50:287–310.
35. Cheng Y, Ma E (2011) Atomic-level structure and structure–property relationship in metallic glasses. *Prog Mater Sci* 56:379–473.
36. Falk ML, Langer JS (2011) Deformation and failure of amorphous, solidlike materials. *Annu Rev Condens Matter Phys* 2:353–373.
37. Langer J (2015) Shear-transformation-zone theory of yielding in athermal amorphous materials. *Phys Rev E* 92:012318.
38. Hufnagel TC, Schuh CA, Falk ML (2016) Deformation of metallic glasses: Recent developments in theory, simulations, and experiments. *Acta Mater* 109:375–393.
39. Langer J (2017) Yielding transitions and grain-size effects in dislocation theory. *Phys Rev E* 95:033004.
40. Kamrin K, Bouchbinder E (2014) Two-temperature continuum thermomechanics of deforming amorphous solids. *J Mech Phys Sol* 73:269–288.
41. Chattoraj J, Caroli C, Lemaître A (2010) Universal additive effect of temperature on the rheology of amorphous solids. *Phys Rev Lett* 105:266001.
42. Kob W, Donati C, Plimpton SJ, Poole PH, Glotzer SC (1997) Dynamical heterogeneities in a supercooled Lennard-Jones liquid. *Phys Rev Lett* 79:2827–2830.
43. Hoffmann S, et al. (2000) Origin of dynamic heterogeneities in miscible polymer blends: A quasielastic neutron scattering study. *Phys Rev Lett* 85:772–775.
44. Becker T, Smith JC (2003) Energy resolution and dynamical heterogeneity effects on elastic incoherent neutron scattering from molecular systems. *Phys Rev E* 67: 021904.
45. Jensen HJ (1998) *Self-Organized Criticality: Emergent Complex Behavior in Physical and Biological Systems* (Cambridge Univ Press, Cambridge, UK), p 126.
46. Gruber M, Abade GC, Puertas AM, Fuchs M (2016) Active microrheology in a colloidal glass. *Phys Rev E* 94:042602.
47. Antonaglia J, et al. (2014) Bulk metallic glasses deform via slip avalanches. *Phys Rev Lett* 112:155501.
48. Fan Y, Yildiz B, Yip S (2013) Analogy between glass rheology and crystal plasticity: Yielding at high strain rate. *Soft Matter* 9:9511–9514.
49. Kushima A, et al. (2009) Computing the viscosity of supercooled liquids. *J Chem Phys* 130:224504.
50. Cao P, Li M, Heugle RJ, Park HS, Lin X (2012) A self-learning metabasin escape algorithm and the metabasin correlation length of supercooled liquids. *Phys Rev E* 86:016710.
51. Henkelman G, Uberuaga B, Jonsson H (2000) A climbing image nudged elastic band method for finding saddle points and minimum energy paths. *J Chem Phys* 113:9901–9904.
52. Shimizu F, Ogata S, Li J (2007) Theory of shear banding in metallic glasses and molecular dynamics calculations. *Mater Trans* 48:2923–2927.

Supporting Information

Cao et al. 10.1073/pnas.1708618114

SI Characterization of Model Metallic Glass

We estimate the glass transition temperature of the model metallic glass by looking at the volume and potential energy changes during cooling. The high-temperature liquid is quenched at zero pressure and a cooling rate of 0.14 K/ps. In Fig. S1*A*, we plot system volume as a function of temperature at constant zero pressure. An apparent glass transition temperature of $T_g \sim 440$ K is observed from the cooling curve. Similarly, the transition temperature is also seen in the potential energy vs. temperature behavior as shown in Fig. S1*B*. An example of quenched metallic glass structure is shown in Fig. S2.

The mechanical properties of the metallic glass, such as Young's modulus and yield stress, are calculated using conventional quasistatic tension simulation. A small strain increment of 10^{-4} is applied in the horizontal direction, and potential energy minimization is performed at the fixed strain. We repeat the procedure until 16% tensile strain. Fig. S3 presents the stress and strain behavior of the model metallic glass. The stress-strain curve shows an essentially linear regime followed by plastic yielding at 4.3 GPa and a subsequent plastic flow regime. We fit the elastic part of the curve. From the slope we extract a modulus ~190 GPa.

SI Evolution of Atomic Strains During Three Stages of Creep

From the corresponding atomic configurations along the evolution trajectory, we extract details of the collective rearrangements in the different creep stages. An example of the spatial distribution of local atomic strains is shown in Fig. S4. Each panel shows the cumulative strains from the start of simulation up to the time indicated. A shear transformation deformation (STD) event is identified by a local strain measure of significant magnitude. Two strain measures are shown in Fig. S4: the von Mises strain η_{Mises} and deviatoric strain D^2_{Min}. Comparison with the strain evolution through the three stages of creep shows clearly the behavior of STD. In the primary stage (less than 1% strain), one sees only a few events appearing randomly. In the secondary stage (around 2% strain), shear transformations occur in sufficient numbers that different sites begin to interact with each other. At about 3% strain (tertiary stage), an incipient localized structure spanning the entire system can be observed. Closer comparison of the two strain measures shows the η_{Mises} distribution to be relatively more continuous and smooth. Since we are interested in identifying the plastic deformation mechanisms, we will focus on D^2_{Min} as the more discriminating indicator.

SI Determination of Mechanism Boundary on Creep Map

Diffusional Flow (High *T*, Low σ). Let us define a parameter $Q_{\rm d}$, representing the activation barrier for atom diffusion at zero external force. When a tensile stress σ is applied, the forward activation barrier becomes smaller than the backward barrier. The atomic diffusion is biased in the tensile direction, and forward diffusion is much faster, which results in driven diffusion flow. At steady-state condition, the creep rate $\dot{\varepsilon}$ can be written as (10)

$$\dot{\varepsilon} = \gamma_0 \exp\left(-\frac{Q_d}{kT}\right) \sinh\left(\frac{\sigma V_d}{KT}\right), \qquad \text{[S1]}$$

where γ_0 is the numerical factor and V_d is the activation volume. At high temperature and low stress ($\sigma V_d \ll KT$), the above equation becomes

$$\dot{\varepsilon}_d = \gamma_0 \exp\left(-\frac{Q_d}{kT}\right) \frac{\sigma V_d}{kT}. \qquad \text{[S2]}$$

The creep rate $\dot{\varepsilon}$ is linearly proportional to stress σ, indicating Newtonian fluid behavior at the limiting high-temperature and low-stress condition.

STD (Low *T*, High σ). The shear transformation operation is the mechanism occurring at low temperature and high stress. We define activation barrier Q_{st} for a shear transformation nucleation at zero applied stress. At finite external stress, the activation barrier is a decreasing function of stress $Q = Q_{st} - \sigma V_{st}$, where V_{st} is activation volume of shear transformation (8, 11). The strain rate can be written as

$$\dot{\varepsilon}_{st} = \gamma_0 \exp\left(-\frac{Q_{st} - \sigma V_{st}}{kT}\right). \qquad \text{[S3]}$$

Determine the Mechanism Boundary. The steady-state strain rates are described in Eqs. **2** and **3** by two atomistic mechanisms: atomic diffusion and STD. Each mode determines the deformation rate at certain temperature and stress conditions. We determine the mechanism boundary between diffusional flow and STD creep by setting $\dot{\varepsilon}_d(T,\sigma) = \dot{\varepsilon}_{st}(T,\sigma)$.

Let us first look at how to determine a mechanism boundary for a case of constant temperature. Assuming the activation energy $Q_d = 1$, $kT = 0.05$, and prefactor $\gamma_0 = 1$ of Eq. **2**, we are able to calculate $\dot{\varepsilon}_d$ as a function σV_d (circles shown in Fig. S5). Computing the strain rate $\dot{\varepsilon}_{st}$ in Eq. **3** requires the shear transformation activation energy Q_{st}. Since we are interested in $\dot{\varepsilon}_{st} = \dot{\varepsilon}_d$, Q_{st} is treated parametrically in a numerical analysis. We find that, when $Q_{st} = 1.051$, the $\dot{\varepsilon}_{st}$ (squares in Fig. S5) is starting to touch $\dot{\varepsilon}_d$. We then determine the cross point, showing the boundary of two mechanisms to be $\sigma V = 0.054$.

Similarly, we calculate the mechanism boundaries at different temperatures, which are shown in Fig. S6. As temperature increases, the critical stress points determining the mechanism cross-over also increase. We plot the values of the critical stress as a function of temperature in Fig. S7 and find that the calculated boundary is a linear line. Thus, the mechanism boundary is determined by the two limiting mechanisms: high T and low σ diffusion flow and the STD occurring at low T and high σ. It separates the stress–temperature map into two regimes, in which one or the other mechanism predominates.

SI Discussion of Cooling Rate Effects on Creep Mechanism Boundary

It is known the potential energy landscape of glasses depends on the cooling rate, which in turn, can influence their creep behavior. To understand the cooling rate effects, we prepare another system of 25,000 atoms at a much higher rate of 140 K/ps, three orders faster in comparison with 0.14 K/ps. We follow the same procedure in applying tensile stress to the system and measuring steady-state creep rate $\dot{\varepsilon}$ at various stresses. Fig. S8 presents $\dot{\varepsilon}$ as a function of stress for the two systems. We see the same bimodal behavior in the variation of creep rate $\dot{\varepsilon}$ with stress σ for both systems, implying that the deformational and diffusional creep mechanisms are also operating in the high-cooling rate system. It is worth noting that the characteristic stress value for the change in index n at the high cooling rate is smaller than that at the low cooling rate. This implies that a lower characteristic (cross-over) stress is involved in the creep rate upturn at a higher cooling rate. Fig. S8 also indicates that creep rates in a high-stress region, associated with STD, are more sensitive to the cooling rate than those in a low-stress region, associated with atomistic diffusion. This is reasonable, since

collective responses are expected to be more sensitive to mid- to long-range ordering in the glass structure (with significant influences from cooling rates) in contrast to atomistic diffusion, which is mostly sensitive to short-range ordering (35).

Fig. S9 shows the comparison of the creep mechanism map for the two systems. The simulation results display the same predominant domains of diffusional and deformational creep, and it should be noticed that the mechanism boundary (dashed lines in Fig. S9) shifts downward when increasing cooling rate. Since the cooling rate in the simulation is invariably higher than experiment, we can expect a shift, such as that indicated qualitatively in Fig. 7, to be present when comparing the two.

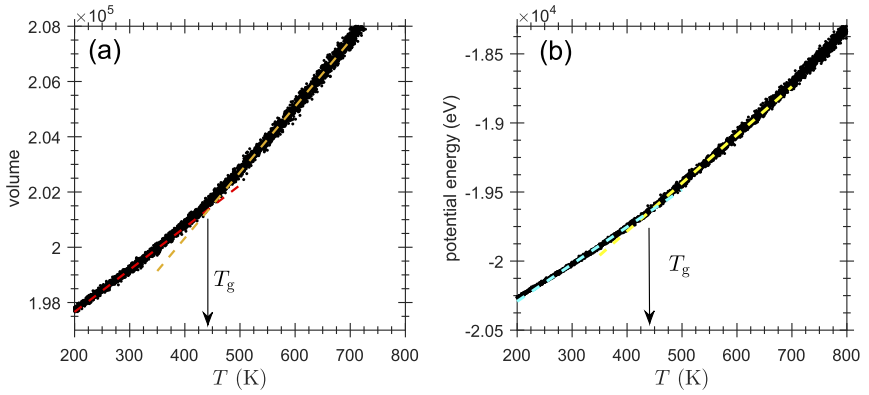

Fig. S1. System volume (*A*) and potential energy (*B*) vs. temperature during cooling at a rate of 0.14 K/ps. The dashed lines are shown with guidelines for glass transition ($T_g \sim 440$ K).

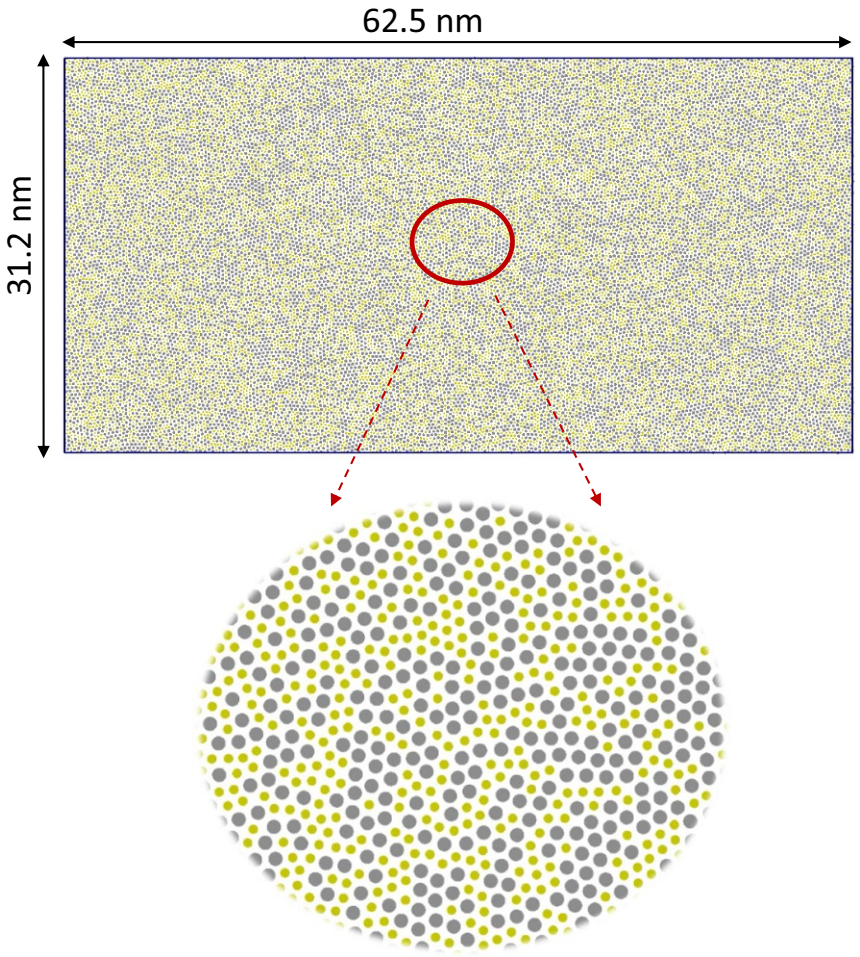

Fig. S2. Atomic structure of the metallic glass containing 25,000 atoms at 300 K. The yellow and gray atoms indicate copper and zirconium, respectively.

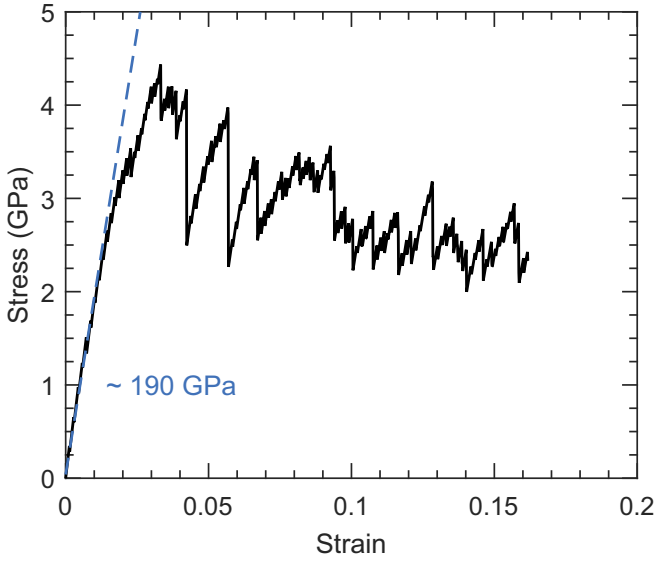

Fig. S3. The solid line is stress as a function of tensile strain produced by quasistatic simulation. The elastic modulus of 190 GPa is obtained by fitting the linear regime of the stress–strain curve (blue dashed line).

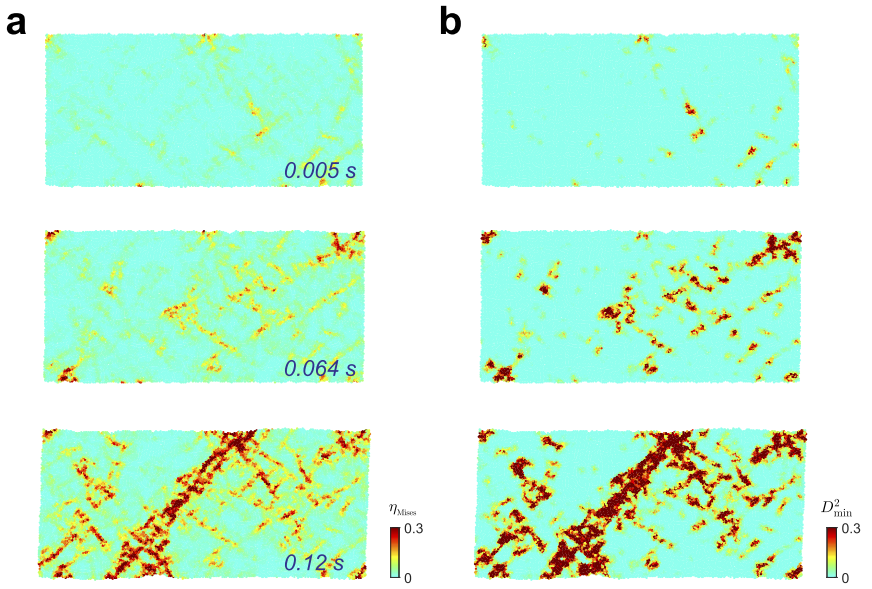

Fig. S4. Spatial distribution of η_{Mises} (*A*) and D^2_{Min} (*B*) during three stages of creep: primary ($t = 0.005$ s, $\varepsilon \sim 0.8\%$), secondary ($t = 0.064$ s, $\varepsilon \sim 2\%$), and tertiary ($t = 0.12$ s, $\varepsilon \sim 3\%$). The atomic strains shown are cumulative results by taking the initial configuration to be the reference. The applied stress is 198 MPa, and temperature is $T = 0.68T_g$. The corresponding creep curve is shown in Fig. 1.

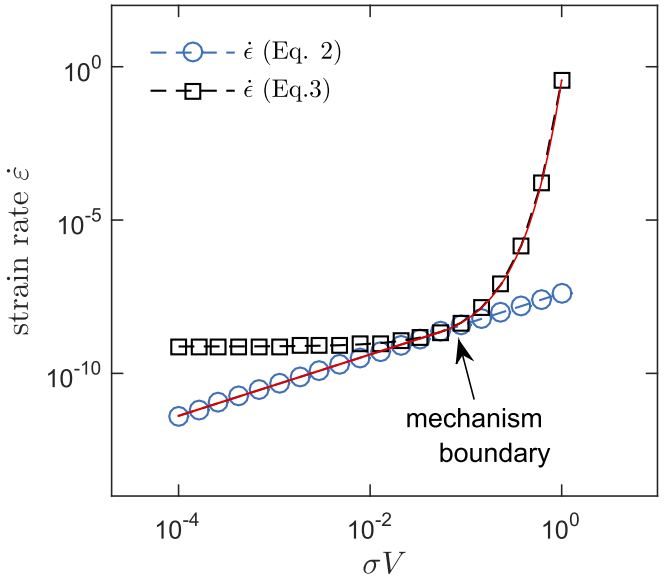

Fig. S5. Theoretically predicted stress-dependent strain rate at temperature $kT = 0.05$. The circles are calculated values using Eq. **S2**, while the squares present strain rate of Eq. **S3**. The cross point is the mechanism boundary, and the red solid line represents the strain rate variation with stress endorsed by mechanism cross-over.

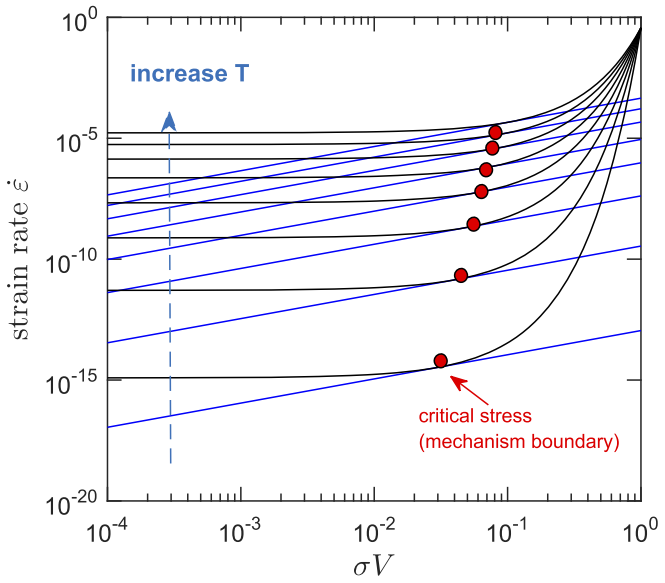

Fig. S6. Theoretically predicted stress-dependent strain rate at different temperatures. The critical stress (mechanism boundary; red dots) increases with increasing temperature.

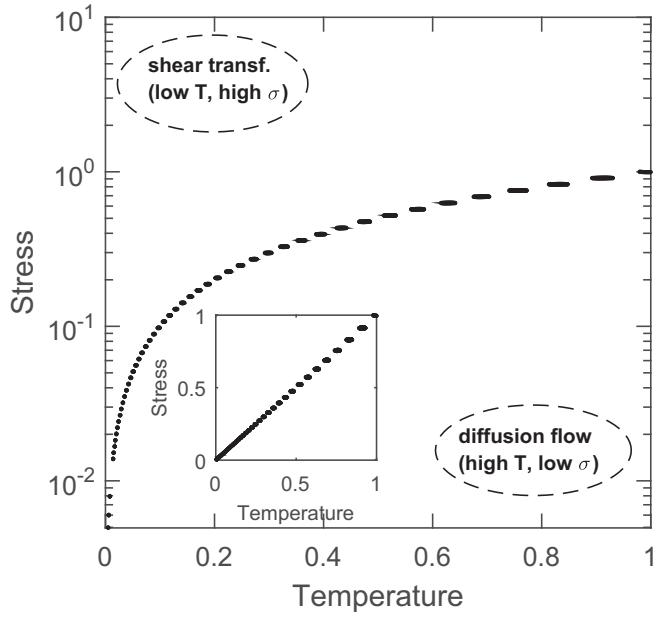

Fig. S7. Theoretically predicted creep mechanism map. The dashed line $\sigma\,(T) = aT$ indicates the mechanism boundary separating the two limiting behaviors: diffusion flow and shear transformation deformation. *Inset* shows the boundary $\sigma(T)$ in linear scales.

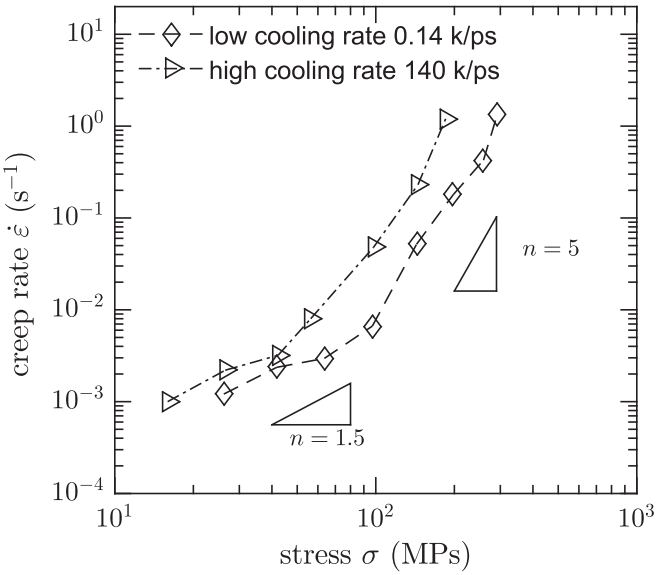

Fig. S8. Stress dependence of steady-state $\dot{\varepsilon}$ from two simulation systems prepared at different cooling rates.

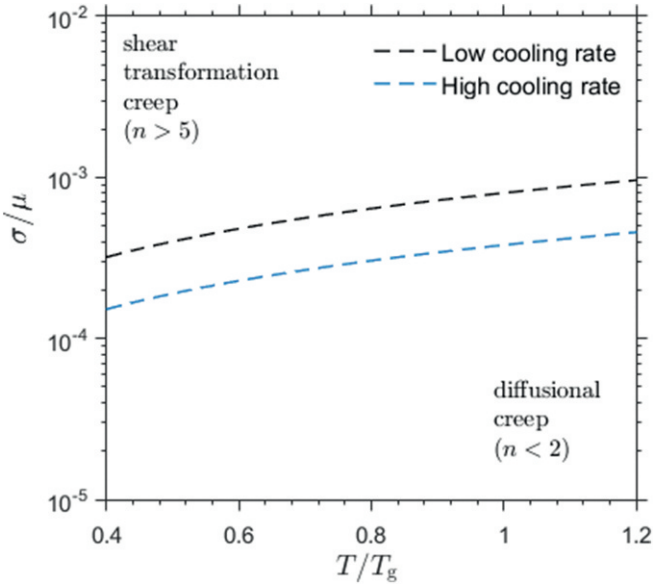

Fig. S9. Creep mechanism map obtained for two different cooling rates. The black dashed line represents mechanism boundaries for the low cooling rate of 0.14 K/ps, while the blue dashed line denotes the high cooling rate of 140 K/ps.